Scientific Reports

https://doi.org/10.1038/s41598-026-44418-3

Article in Press

Topotactic engineering of high-entropy (oxy) hydroxide nanotubes for enhanced photocatalysis

Received: 21 December 2025

Accepted: 11 March 2026

Published online: 19 March 2026

Cite this article as: Pacheco-Espinoza S., Hernández-Pérez M.Á., Cuesta-Balderas A.I. *et al.* Topotactic engineering of high-entropy (oxy) hydroxide nanotubes for enhanced photocatalysis. *Sci Rep* (2026). https://doi.org/10.1038/s41598-026-44418-3

Sarahi Pacheco-Espinoza, María Ángeles Hernández-Pérez, Alejandro Iván Cuesta-Balderas, Alejandra Verdejo-Palacios, Raúl Borja-Urby & Jorge Roberto Vargas-García

Topotactic Engineering of High-Entropy (Oxy)hydroxide Nanotubes for Enhanced Photocatalysis

Sarahi Pacheco-Espinoza[1,*], María Ángeles Hernández-Pérez[1,+], Alejandro Iván Cuesta-Balderas[1,+], Alejandra Verdejo-Palacios[1,+], Raúl Borja-Urby[2,+], and Jorge Roberto Vargas-García[1,*]

[1]Instituto Politécnico Nacional, Depto. Ing. Metalurgia y Materiales, Ciudad de México, 07738, México
[2]Instituto Politécnico Nacional, Centro de Nanociencias y Micro y Nanotecnologías, Ciudad de México, 07738, México
*Corresponding author E-mail: rvargasga@ipn.mx
*Corresponding author E-mail: sarahi.p.e@hotmail.com
[+]these authors contributed equally to this work

ABSTRACT

This study introduces a novel topotactic synthesis method for CeCoNiAlGa high-entropy oxyhydroxide (HE-OOH) nanotubes utilizing multiwalled carbon nanotubes (MWCNTs) as the parent crystal. This approach yields concentric nanotubes with high crystalline order and a fluorite-like structure supported by a distorted Ce–O framework. Neutral M–OH–M sheet stacking, resembling dehydrated brucite-like layers, governs the multiwalled configuration, with topotactic alignment between fluorite-like (111) and carbon (002) planes. Controlled heat treatment (80 – 600 ºC) induces gradual dehydroxylation while preserving the multiwalled morphology and sole fluorite-like structure up to 500 °C, confirming CeCoNiAlGa HE-OOH as direct precursors of high-entropy oxides (HEOs). In CeCoNiAlGa nanotubes, the elevated number of oxygen vacancies compensates for the charge imbalance arising from multiple cations, and dehydroxylation enhances collective charge redistribution, thereby increasing the vacancy concentration. CeCoNiAlGa HE-OOH nanotubes obtained at 80 ºC exhibit superior photocatalytic performance, achieving 96% ciprofloxacin (CIP) degradation in 45 min following pseudo-second-order kinetics (k = 0.71 L/mg•min). Scavenger studies identify

photogenerated holes as the dominant reactive species, while abundant surface hydroxyl groups facilitate interfacial charge transfer and reactive radical formation, enhancing photocatalytic efficiency. These findings establish CeCoNiAlGa HE-OOH as a structural precursor for enhanced photocatalytic performance through controlled topotactic and electronic-structure engineering.

Keywords: High-entropy materials; Topotactic transformation; Nanostructured catalysts; Environmental photocatalysis; Ciprofloxacin photodegradation

Introduction

In recent years, HEOs have emerged as promising candidates for advanced energy storage and catalytic applications.[1-5] The synergistic effects arising from their multiple cations enable the tailoring of physicochemical properties to meet the demands of the application.[6] So far, a considerable number of significant studies have demonstrated that HEOs form a single-phase and well-defined crystal structure, such as rock salt $(Co_{0.2}Cu_{0.2}Mg_{0.2}Ni_{0.2}Zn_{0.2})O$, spinel $(Co_{0.2}Cr_{0.2}Fe_{0.2}Mn_{0.2}Ni_{0.2})_3O_4$, perovskite $Ba(Zr_{0.2}Sn_{0.2}Ti_{0.2}Hf_{0.2}Nb_{0.2})O_3$, and fluorite $(Ce_{0.2}La_{0.2}Pr_{0.2}Sm_{0.2}Y_{0.2})O_{2-\delta}$ types.[7-10] Closely related, HE-OOHs also signify a rapidly advancing area of research with significant potential in electrocatalytic applications. Albeit an evolving area, distinct structural patterns for HE-OOHs are primarily recognized as orthorhombic, tetragonal, and octahedral layered stacks.[11-12] Additionally, significant efforts have been devoted to developing synthesis methods to expand the functionalities of HEOs, leading to nanostructured HEOs in the form of nanoparticles, nanofibers, and porous structures.[13-20] However, HEO nanotubes have been rarely achieved despite their promising benefits of enhanced surface area and

exposure of desirable crystallographic planes. [21,22] Traditional synthesis methods for HEOs and HE-OOHs, although well-established and yielding high-quality results, still restrict the precise control of morphology and nanostructure features.[23] Furthermore, research delving into technologies that operate beyond the common compositions of HEOs, exploring innovative designs and functionalities, is even scarcer. The topotactic transformation offers an attractive route for achieving highly desirable structures. The topotactic transformation is a solid-state transformation where a parent crystal converts into a pseudomorph, maintaining its crystallographic orientation and morphology.[24] Inspired by our previous investigations concerning $CeO_{2-\square}$ nanotubes, the current research explores the feasibility of generating novel CeCoNiAlGa HE-OOH multiwalled nanotube structures.[25] This is accomplished via topotactic transformation utilizing MWCNTs as the parent crystal. Single-phase HE-OOHs incorporating the unprecedented combination of Ce-Co-Ni-Al-Ga cations have not been previously reported, and their properties remain unexplored. This novel combination is intended to leverage the Ce^{3+}/Ce^{4+}, Co^{2+}/Co^{3+}, Ni^{2+}/Ni^{3+} redox couple activity, Ce ability for fluorite-structure stabilization, synergistic catalytic effects of Co-Ni, and the potential for structural/electronic promotion of Al-Ga. We demonstrate the application of CeCoNiAlGa HE-OOH nanotubes as a catalyst for the CIP photodegradation. The distinctive features of CeCoNiAlGa HE-OOH nanotubes produced through the topotactic method include a high density of surface hydroxyl groups, which boosts photocatalytic performance.

Results and Discussion

The CeCoNiAlGa HE-OOH nanotubes are referred to as OHNTs. **Table 1** presents a summary of sample identification. **Figure 1a** depicts typical X-ray diffraction (XRD) patterns of *f*-MWCNTs and topotactically grown products (OHNTs). The XRD pattern of *f*-MWCNTs shows distinctive diffraction peaks of

the graphite structure at 2θ = 26.06° and 43.60° (JCPDS 041-1487). Besides the small C (002) peak, the XRD patterns of OHNTs exhibit broad peaks close to those of the CeO_2 cubic fluorite structure (JCPDS 34-0394). Although OHNTs do not adopt the ideal cubic fluorite symmetry, the peak proximity suggests a distorted Ce-O framework that is derivative of the fluorite structure. The C (002) and OHNTs (111) peaks were analyzed by deconvolution analysis. **Figure 1b** shows that the OHNTs (111) peak was fitted by two Gaussian curves based on CeO_2 and $Ce(OH)_3$ (JCPDS 019-0284). This confirms the coexistence of dual-phase structures that we interpret as oxy(hydroxides). The fitting analysis reveals, additionally, a temperature-dependent change in the oxide/hydroxide ratio. From 400 °C, the oxide phase dominates. Configurational entropy may enable the unusual cationic combination of Ce, Co, Ni, Al, and Ga to form a HE-OOH with a fluorite-like structure that remains stable up to 500 °C. The broadening of diffraction peaks may indicate structural disorder and small crystalline regions. A broad and negligible peak corresponding to NiCoxOx emerges at 600 °C, which corresponds to a secondary phase.

Table 1. Identification of samples.

CeCoNiAlGa HE-OOH nanotubes	Heat-treatment temperature (ºC)
$OHNT_{80}$	80 (dried)
$OHNT_{400}$	400
$OHNT_{500}$	500
$OHNT_{600}$	600

The minor C (002) peak in the OHNTs diminishes quickly as the temperature rises. The optimal fit for the C (002) peak was achieved using two Gaussian curves, associated with Bernal (□-curve) and non-Bernal (□-curve) stacking orders commonly found in MWCNTs.[26,27] According to the integrated intensities of □- and □-curves, the relative intensity of non-Bernal stacking

order increased upon forming OHNTs. The increased structural disorder may be attributed to the intercalation of cations (Ce, Co, Ni, Al, Ga) between adjacent graphene layers of parent *f*-MWCNTs. As previously observed for $CeO_{2-\square}$ NTs, OHNTs may grow topotactically after an initial stage of cation intercalation into the *f*-MWCNTs wall spacing.[25,28] A small fraction of intercalated *f*-MWCNTs may remain unchanged, associated with the small C (002) peak exhibiting a primary $\square$ component. The topotactic synthesis demonstrates its ability to produce single-phase fluorite-like CeCoNiAlGa HE-OOHs at relatively low temperatures (80-500 °C).

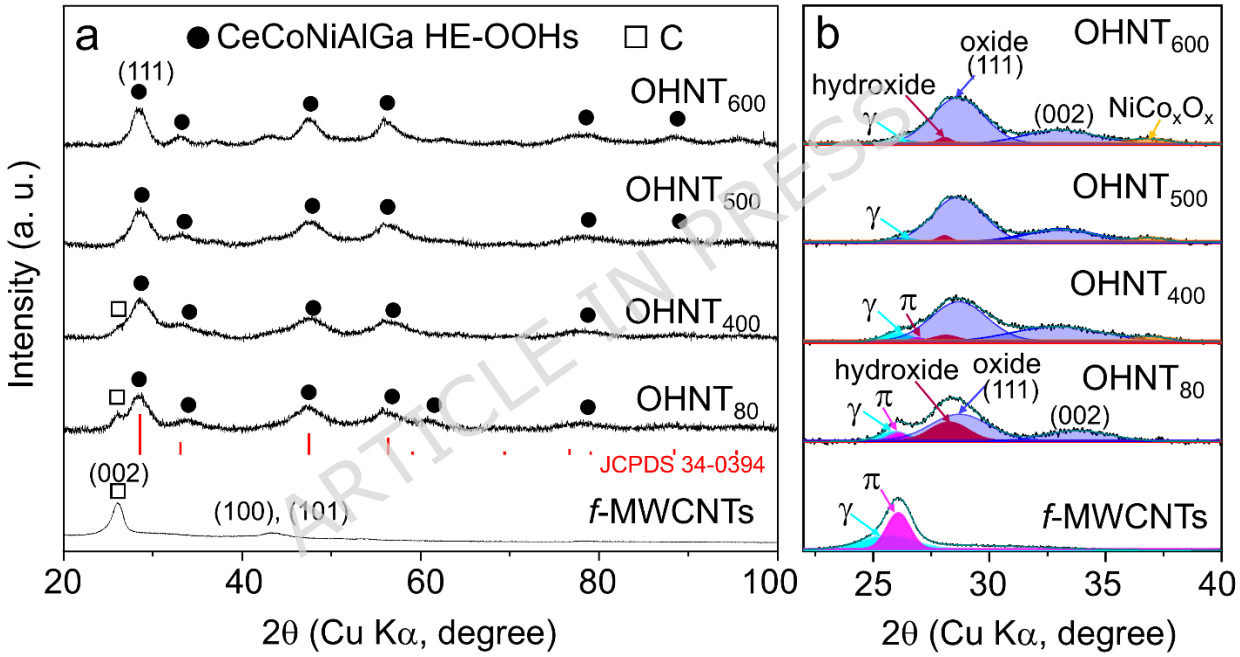

Figure 1. a) XDR patterns of *f*-MWCNTs and OHNTs, b) deconvolution analysis of
C (002) and OHNTs (111) XRD peaks.

Figures 2 (a-b) show the High-Resolution Transmission Electron Microscopy (HR-TEM) images of *f*-MWCNTs and $OHNT_{400}$. These images demonstrate that the main characteristic of $OHNT_{400}$ is their well-organized crystalline tubular structure with a concentric cylindrical layer configuration, analogous to parent *f*-MWCNTs. The fast Fourier transform patterns display spots corresponding to

the *f*-MWCNTs C (002) planes and $OHNT_{400}$ (111) planes, respectively. The parent crystal and its pseudomorph share a common tube axis, with the normals to the C (002) or $OHNT_{400}$ (111) planes oriented perpendicular to the axis. This strongly suggests that the $OHNT_{400}$ has grown topotactically on the MWCNTs, with the $OHNT_{400}$ [111] direction oriented normal to the curved C (002) planes. Such a crystallographic relationship should be consistent with favorable lattice matching between the two phases, arising from their compatible hexagonal symmetry. In consequence, the $OHNT_{400}$ (111) planes are preferentially aligned parallel to the nanotube surface. The shape and orientation of the parent crystal are effectively inherited despite significant compositional changes during the topotactic transformation. Nevertheless, as shown in **Figure 2c**, local misalignments are noted throughout the multiwalled configuration. These defects may primarily result from variations in composition and/or stress due to the curved shape. Large discontinuity of the tubular morphology is also evident in $OHNT_{400}$. Such a process appears to result in shorter tubes that eventually collapse into irregular particles as heat-treatment temperature increases. In addition, individual randomly oriented crystalline particles are observed on the surface of $OHNT_{400}$ nanotubes, suggesting an excess of multicationic precursors during synthesis. Despite the measurement uncertainty, the interlayer spacing of OHNTs is uniform in the radial direction. In $OHNT_{400}$, it is about 0.37 nm, showing that the topotactic transformation occurs throughout the parent *f*-MWCNTs volume. The interlayer spacing of 0.37 nm is consistent with a partially dehydrated brucite-like layered hydroxide structure composed of neutral M–OH–M sheets.[29] In such a layered structure the stacking is maintained by weak interlayer interactions. This condition may account for the structural flexibility required to arrange curved HE-OOH (111) layers with progressively larger diameters into a multiwalled nanotube. **Figures 2 (c-d)** display the HR-TEM image of an individual $OHNT_{400}$ along with its corresponding local electron energy loss spectroscopy (EELS) elemental mapping image. The detection of cerium,

cobalt, nickel, aluminum, gallium, and oxygen confirms the presence of a Ce-Co-Ni-Al-Ga-O chemical system in the topotactically grown $OHNT_{400}$.

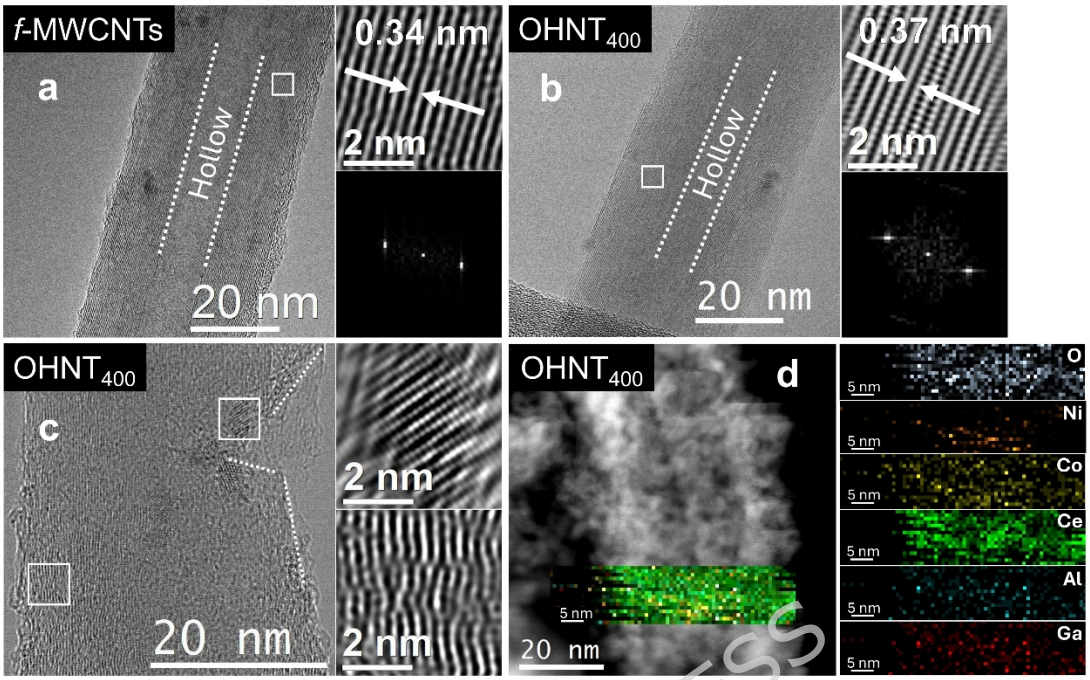

Figure 2. HR-TEM images of a) *f*-MWCNTs, b-c) $OHNT_{400}$, and d) EELS elemental mapping image.

The Raman spectra for *f*-MWCNTs and OHNTs are depicted in **Figure 3a**. The Raman spectra of OHNTs exhibit the distinctive F_{2g} band reported for the cubic fluorite structure at ≈ 447 cm^{-1}, which rises in intensity with increasing heat-treatment temperature. The F_{2g} band shows broadening and a shift to lower frequencies relative to CeO_2 NPs. [30] The significant shift of ≈ 23 cm^{-1} and concurrent broadening are ascribed to the distorted structure of OHNTs. The unusual combination of Al, Co, Ni, and Ga cations in a fluorite-like structure leads to significant O vacancies, as indicated by bands in the 500-700 cm^{-1} range.[31] The spectra of $OHNT_{80}$ and $OHNT_{400}$ additionally show distinguishable D, G, and 2D bands of the graphitic structure, indicating the presence of graphitic domains in OHNTs. The G band exhibits a characteristic shoulder associated with lattice distortion caused by intercalated heteroatoms.[32] This may be attributed to the small, residual fraction of multicationic intercalated *f*-MWCNTs in OHNTs. $OHNT_{500}$ exhibits no graphitic bands, in agreement with previous analyses.[25]

Raman spectra of OHNTs were deconvoluted using a combination of five to six bands (D_1-D_6), incorporating the model proposed by Sartoretti et al.[30] **Figure 3b** depicts the curve-fitting analysis of the F_{2g} band. The D_3 band, assigned to the F_{2g} first-order symmetric stretching of the fluorite lattice, appears between 441-455 cm^{-1}.[30] This is shifted to a lower wavenumber relative to bulk CeO_2 (≈ 460-465 cm^{-1}), consistent with the defect-induced lattice of OHNTs. The D_1 (≈ 310-330 cm^{-1}) is attributed to the 2TA second-order scattering originating from lattice anharmonicity and disorder.[33] The D_4, D_5, and D_6 bands are characteristic of defect-related local modes. The D_4 has been assigned to O vacancies coupled with reduced Ce^{3+} or aliovalent cations.[34] D_5 is commonly attributed to Frenkel-pair/O-vacancy environments or to aliovalent-containing defect regions.[35,36] The D_6 band is associated with extrinsic defects introduced by aliovalent cations and reflects the formation of MO_8 units in the absence of O vacancies (M = aliovalent cation).[36] The D_2 band represents the breathing mode of Ce-O framework in OHNTs.[37,38] The progressive upward shifts of several defect bands and the F_{2g} position in $OHNT_{600}$ suggest changes in the local Ce–O bonding and defect density due to the incremental dehydroxylation in OHNTs. Supplementary **Table S1** summarizes the identification of first- and second-order Raman bands.

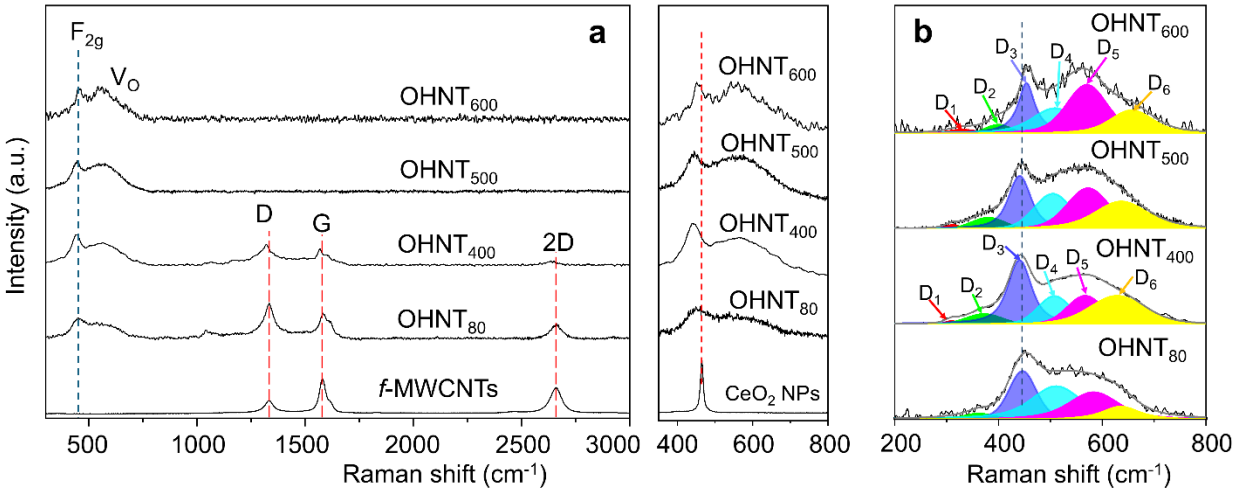

Figure 3. a) Raman spectra of *f*-MWCNTs and OHNTs, b) deconvolution analysis of the F_{2g} band.

Figure 4a displays the X-ray Photoelectron Spectroscopy (XPS) survey spectra of OHNTs, which unequivocally confirm the presence of C, as well as Ce, Co, Ni, Al, and Ga elements. The spectra show a decrease in C 1s peak intensity with increasing temperature, consistent with previous analytical findings. **Figure 4b** illustrates a comparison of high-resolution C 1s spectra for *f*-MWCNTs and OHNTs. OHNTs exhibit a notable broadening of the C 1s peak and an increase in intensity in the C-O (≈ 286.6 eV) and C=C-OH (≈ 288.1 eV) regions, indicative of graphitic phase degradation. The broadening corresponds to a notable increase in sp^3 hybridization, which may be associated with amorphous carbon regions that incorporate oxygen-containing functional groups, particularly in the form of polycyclic aromatic-like structures.[25] Under these circumstances, the shift of the sp^2 peak may originate from structural and electronic perturbations caused by the intercalation of cations (Ce, Co, Ni, Al, Ga) into *f*-MWCNTs.

Our findings indicate that Ce-O framework supports the formation and stabilization of the fluorite-like structure in OHNTs. Therefore, the Ce 3d core-level spectra of OHNTs were analyzed, as shown in **Figure 4c**. The Ce peaks from 3d5/2 and 3d3/2 levels (V and u) were observed at 880.0 and 898.7 eV, respectively. Both spin-orbit doublets displayed three corresponding satellite peaks (v′, v″, v‴, u′, u″, and u‴). The high concentration of Ce^{3+} in OHNTs suggests modulation of the electronic structure driven by aliovalent cation substitution.[34] The incorporation of smaller cations (Ni^{2+}: 0.69 Å, Co^{2+}: 0.74 Å, Al^{3+}: 0.53 Å, Ga^{3+}: 0.62 Å) induces lattice strain because of their size difference from Ce^{4+}.[39-43] The high configurational entropy ($\Delta S = 1.6R$) can alleviate the stress, thereby stabilizing the single-phase fluorite-like structure even at relatively low temperatures (80-500 ºC). However, substituting Ce^{4+}

with considerably smaller cations such as Al^{3+} (0.53 Å) restricts phase stability, possibly leading to the secondary phase observed at 600 ºC.

Figure 4d illustrates the high-resolution O 1s spectra for OHNTs. The broad O 1s peak is deconvoluted into four components: lattice O (O_L) at 529.5 eV, O vacancies (O_V) at 531.5 eV, surface-adsorbed oxygen/hydroxyl species (O_A) at 532.0 eV, and chemisorbed water at 533.5 eV. In $OHNT_{80}$, the significant chemisorbed water signal is attributed to a surface passivation mechanism involving water adsorption into O vacancy sites.[44] As temperature rises, the O_V and O_A components exhibit an inverse relationship that aligns with the gradual dehydroxylation in OHNTs, along with the formation of O vacancies.[45] The O_V concentration can be calculated by the ratio, $O_V/(O_L+O_V+O_A)$, as shown in **Figure 4e**. The remarkably high concentration of O vacancies likely compensates for the charge imbalance introduced by the presence of aliovalent cations.[46]

The gradual shift of the O 1s peak toward lower binding energies during dehydroxylation can be attributed to charge transfer from metal cations to oxygen atoms, reflecting the progressive transformation of hydroxyl groups into an M–O–M framework.[47,48] The Ce 3d spectrum demonstrates a shift toward lower binding energy and a decrease in the relative Ce^{3+} contribution, suggesting partial oxidation toward Ce^{4+}, consistent with the formation of a defect-fluorite structure. The metal core-level spectra shown in **Figure S1** exhibit binding-energy shifts and changes in relative contributions, reflecting collective charge redistribution rather than isolated redox processes. This behavior is characteristic of HEOs, where strong metal–oxygen hybridization enables electronic compensation to be distributed across multiple cation species.[49] These findings indicate that dehydroxylation promotes the formation of a structurally integrated HEOs network, in which charge redistribution among multiple cation species stabilizes the highly disordered fluorite structure. **Table S2** presents the results of semi-quantitative chemical

analyses for all OHNTs obtained through EDS and XPS. These analyses indicate that carbon concentrations decrease with increasing temperature, while oxygen and metal atomic percentages increase, reflecting the loss of carbonaceous material. This shift causes metallic elements to achieve a more balanced ratio within the structure, leading to a uniform multicationic distribution typical of high-entropy oxides.

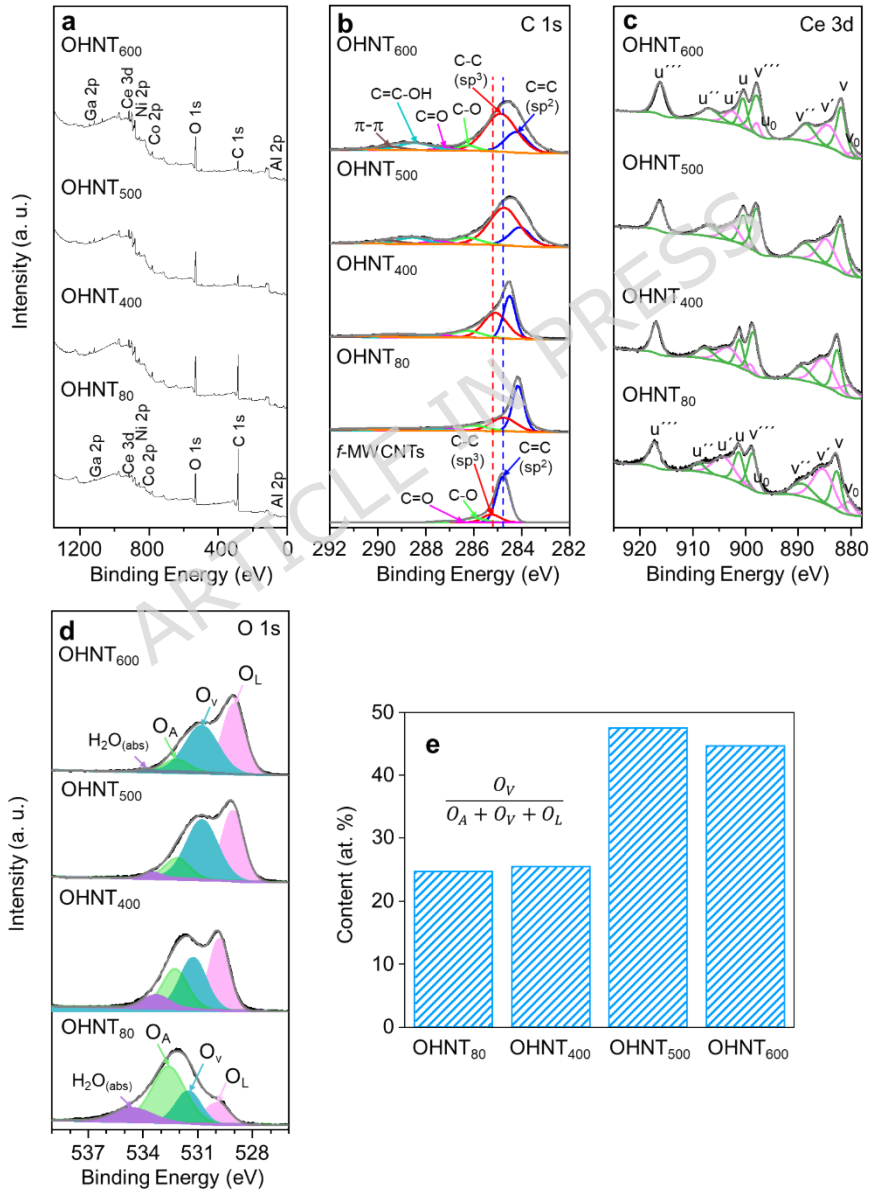

Figure 4. a) Survey spectra for OHNTs, b) high-resolution C 1s spectra for *f*-MWCNTs and OHNTs, c) Ce 3d spectra for OHNTs, d) O 1s spectra for OHNTs, and e) O_V concentration.

The thermal gravimetric analysis (TGA) curves of *f*-MWCNTs and OHNTs in their as-prepared condition are compared in **Figure 5a**. The *f*-MWCNTs exhibit a single weight-loss event of approximately 93% between 500 and 660 °C, typically attributed to combustion, producing CO/CO_2.[50] The solid residue (≈ 7 %) may arise from the Fe synthesis catalyst. In contrast, the OHNTs exhibit a continuous, multi-step weight loss of ≈ 42% from the onset of heating to 510 °C. The corresponding Differential Thermal Analysis (DTA) curve **(Figure 5b)** shows alternating endothermic and exothermic peaks. The first endothermic event occurring below 100 °C is assigned to physisorbed water loss. The subsequent endothermic events at ≈ 1 82, 263, and 500 °C are attributed to stepwise dehydroxylation, which may form complex (oxy)hydroxide intermediates.[51,52] The high-resolution XPS spectra for Co, Ni, Al, and Ga presented in Supplementary **Figure S1** illustrate the complexity of the (oxy)hydroxide transformation during the dehydroxylation process. The exothermic events at ≈ 135, 223, and 402 ºC are consistent with the oxidation of residual C within the OHNTs. No significant weight loss occurs above 550 °C indicating that OHNTs are a direct structural precursor of HEOs.

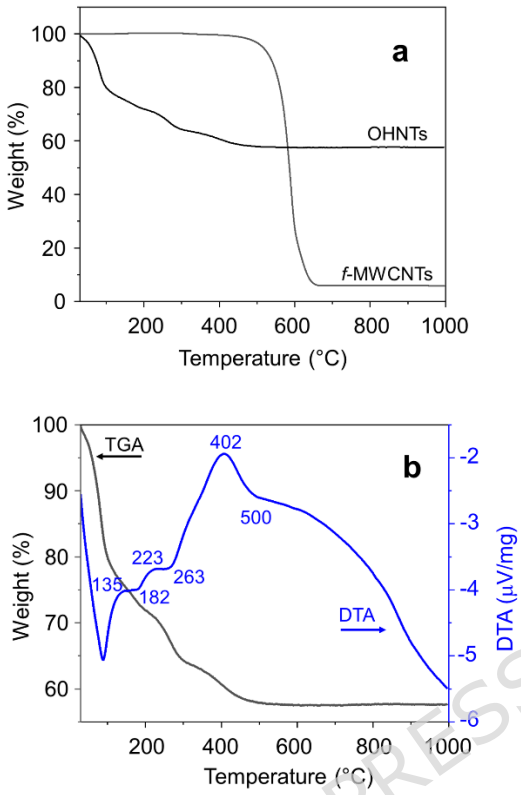

Figure 5. a) TGA curves of *f*-MWCNTs and OHNTs in their as-prepared condition, and b) DTA curve of OHNTs

Figure 6 shows Field Emission Scanning Electron Microscopy (FE-SEM) images depicting the morphological evolution of OHNTs as the temperature increases. At 80 °C, the OHNTs display a clear 1D morphology; however, their stability gradually deteriorates and, above 600 °C, collapses into agglomerated particles.

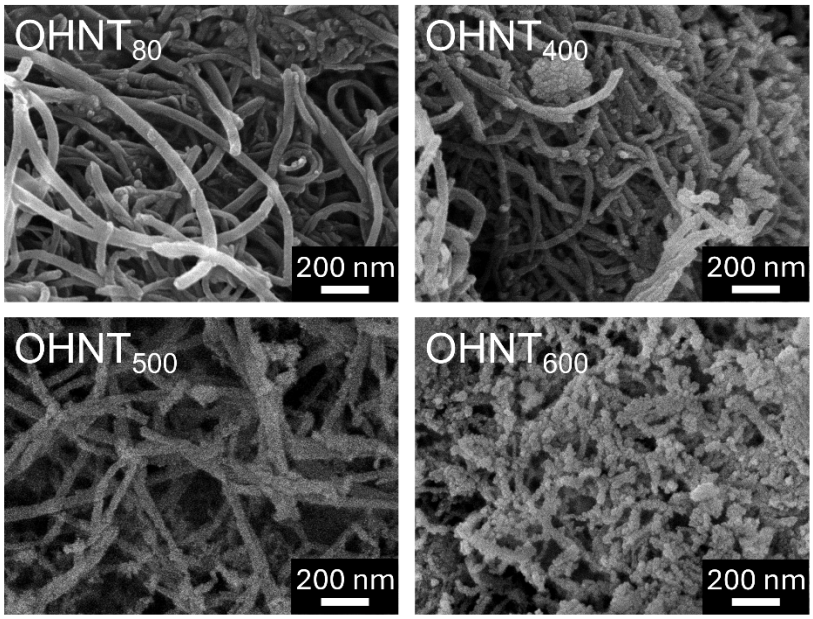

Figure 6. SEM images of the OHNTs morphological evolution.

The photocatalytic performance of OHNTs was assessed by photodegradation of ciprofloxacin (CIP) under UV irradiation (= 365 nm). **Figure S2** shows the UV-vis absorbance spectra for the degradation of CIP over OHNTs. CIP adsorption/desorption equilibrium was reached after the initial 30 min in the dark. The efficiency of OHNTs in photocatalytic CIP degradation is depicted in **Figure 7a**. In the absence of the OHNTs (photolysis), the CIP removal was 36%. The maximum CIP degradation of 96% was attained with $OHNT_{80}$ after 45 min of illumination. The absorption kinetics of CIP on OHNTs were analyzed using pseudo-first order and pseudo-second order models, as shown in **Figures 7b** and **7c**. **Table S3** summarizes the model equations. The comparison of R^2 and k values indicates that the pseudo-second order model yields a closer fit to the experimental data. This suggests that the rate-limiting step of the reaction is the chemisorption of CIP on the surface of the OHNTs. The calculated rate constant of 0.71 L/mg•min for CIP demonstrates the highest removal efficiency among the tested OHNTs.

To elucidate the dominant degradation pathway, scavenger experiments were conducted on $OHNT_{80}$. **Figure 7d** shows the effect of radical scavengers on CIP degradation over OHNTs. The addition of EDTA, a photogenerated hole (h^+) scavenger, significantly suppressed CIP degradation to 47%, clearly identifying h^+ as the primary oxidative species governing the photocatalytic process. This strong inhibition indicates that direct h^+-mediated oxidation is the dominant degradation pathway, likely occurring at the catalyst surface where CIP molecules are adsorbed. When tert-butanol (T-BuOH), a selective hydroxyl radical (•OH) scavenger, was introduced, the degradation efficiency remained relatively high at 85%, indicating that •OH radicals play only a minor role in the overall degradation mechanism. This suggests that •OH-mediated oxidation is not the primary pathway in this system. Similarly, the addition of $AgNO_3$, an electron (e^-) scavenger, resulted in a degradation efficiency of 85%, demonstrating that e^- and electron-mediated reactive oxygen species (ROS) contribute minimally to CIP degradation. In contrast, ascorbic acid, a non-selective scavenger capable of quenching multiple reactive species, reduced the degradation efficiency to 66%, qualitatively confirming the coexistence of secondary ROS, although their overall contribution remains limited compared to h^+-driven oxidation. Based on the relative inhibition observed, the contribution of reactive species follows the order:

$$h^+ > \text{secondary ROS} > (\bullet OH, e^-)$$

These results demonstrate that the photocatalytic degradation of CIP over $OHNT_{80}$ is primarily governed by direct oxidation via h^+, with •OH and e^--mediated pathways playing secondary roles. The dominant role of h^+ underscores the importance of surface hydroxyl groups in facilitating h^+ trapping and interfacial charge transfer, thereby enhancing the oxidation of adsorbed CIP molecules.

UV-vis diffuse reflectance spectrometry (DRS) spectra of $OHNT_{80}$ and $OHNT_{600}$ are shown in **Figure 7e**. The reflectance spectrum for $OHNT_{80}$ does not show a distinct edge in the 200–1100 nm range, suggesting that the optical band gap lies outside the measured range, likely in the infrared region, indicating a narrow bandgap semiconductor. In contrast, a reflectance edge for $OHNT_{600}$ appeared near 620 nm. The energy gap for $OHNT_{600}$ was determined to be 2.0 eV using the Kubelka–Munk method.

Figure 7f depicts the photoluminescence (PL) spectra of $OHNT_{80}$ and $OHNT_{600}$ in the wavelength range of 360–600 nm. Both materials exhibit a maximum emission at approximately 383 nm, followed by a gradual decrease in intensity. $OHNT_{80}$ shows a higher PL intensity compared to $OHNT_{600}$, indicating a higher rate of bulk radiative recombination.[53] However, despite this behavior, $OHNT_{80}$ exhibits superior photocatalytic performance in CIP degradation. This enhanced activity is attributed to the higher concentration of surface hydroxyl groups in $OHNT_{80}$, which act as active sites for trapping h^+ and promoting the formation of reactive •OH. These surface hydroxyl groups facilitate efficient interfacial charge transfer and enhance the oxidation of CIP molecules. In contrast, the dehydroxylated $OHNT_{600}$, although exhibiting lower recombination in the bulk, contains fewer surface reactive sites, resulting in reduced photocatalytic efficiency.

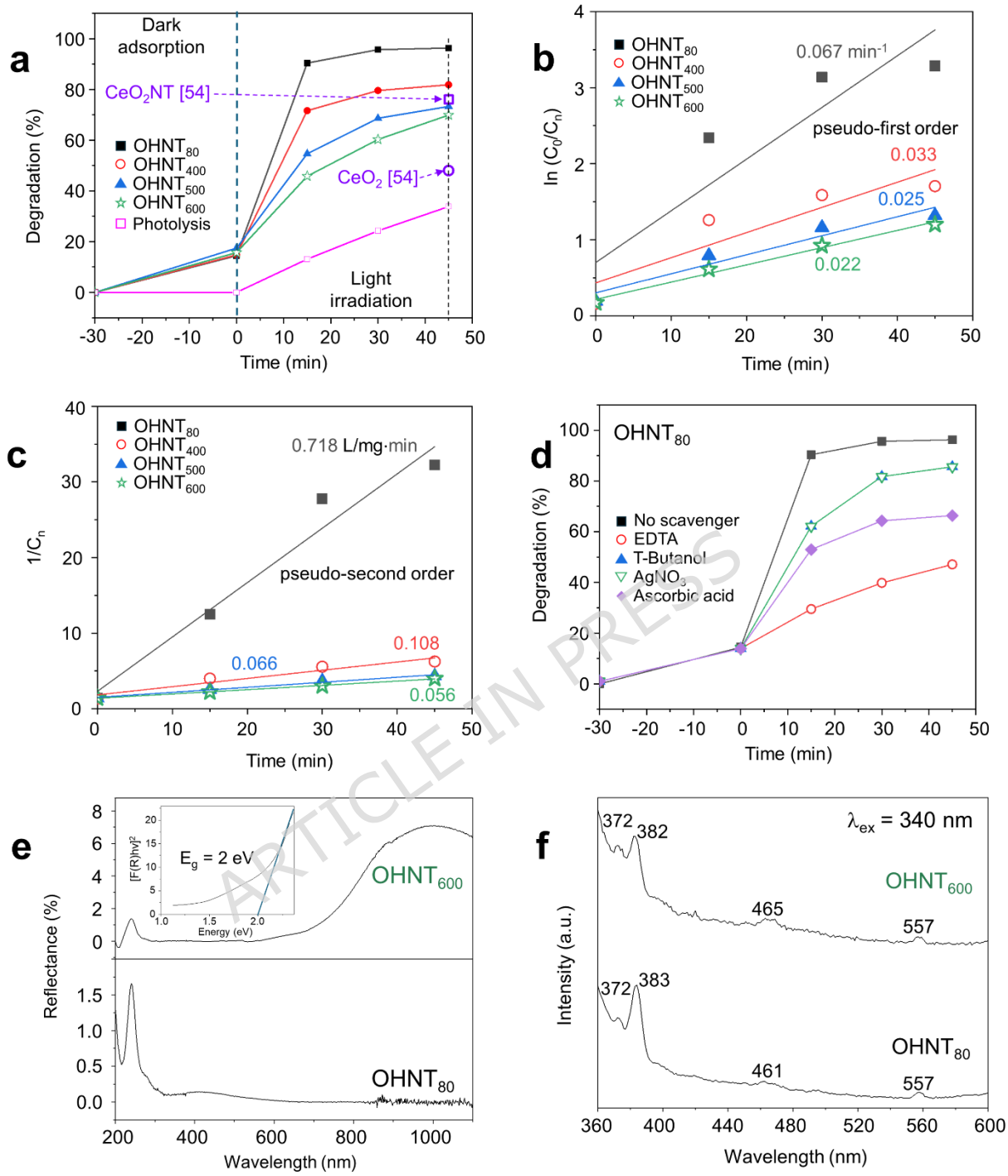

Figure 7. a) Efficiency of OHNTs in photocatalytic CIP degradation, kinetic of CIP degradation using b) pseudo-first order model and c) pseudo-second order model, d) effect of radical scavengers on CIP degradation, e) UV-vis DRS spectra of $OHNT_{80}$ and $OHNT_{600}$, and f) PL spectra of $OHNT_{80}$ and $OHNT_{600}$

Figure 8 illustrates the degradation mechanisms for $OHNT_{80}$ and $OHNT_{600}$, considering their surface chemistry and defect density. In $OHNTs_{80}$, the abundant surface hydroxyl groups facilitate the reaction of h^+, driving direct CIP oxidation and the generation of surface-bound •OH, resulting in a high degradation efficiency (96%).[55] In $OHNT_{600}$, the reduced hydroxyl groups limit h^+-reactive sites, while excessive O vacancies act as deep trap states promoting charge recombination.[56] This suppresses the dominant h^+-driven pathway and shifts the reaction toward less efficient e^--mediated pathways, resulting in a lower overall efficiency (86%).

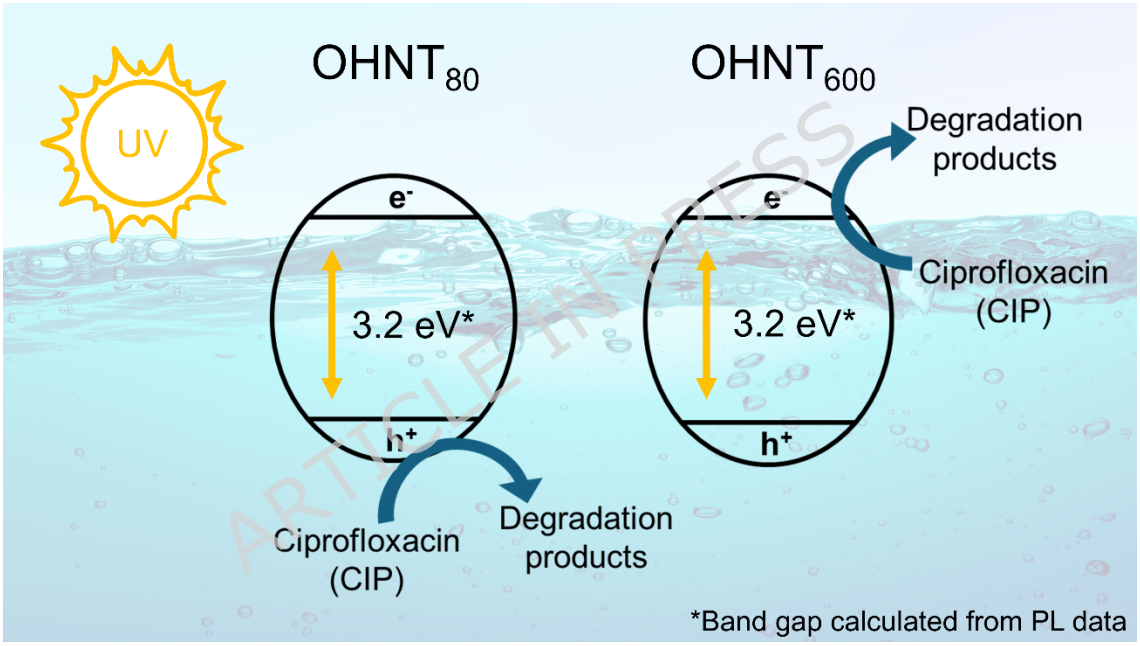

Figure 8. The degradation mechanisms for $OHNT_{80}$ and $OHNT_{600}$

In summary, topotactic synthesis enables the formation of single-phase fluorite-like OHNTs at relatively low temperatures (80–500 °C). The enhanced photocatalytic activity of OHNTs for CIP degradation is due to the higher concentration of surface hydroxyl groups, which act as active sites for trapping h^+ and promoting the formation of reactive •OH radicals. Compared with traditional synthesis methods, topotactic transformation offers superior control over the morphology, composition, and functionality of OHNTs when

favorable crystallographic symmetry alignment exists between the parent and product structures.

Methods

Synthesis of OHNTs

The OHNTs were prepared via an innovative topotactic route in which the entire volume of the parent single-crystalline *f*-MWCNTs was converted into CeCoNiAlGa HE-OOHs pseudomorphs using the conventional liquid-phase deposition method. As-received commercially available $Ce(NO_3)_3{\cdot}6H_2O$, $Al(NO_3)_3{\cdot}9H_2O$, $Co(NO_3)_2{\cdot}6H_2O$, $Ni(NO_3)_2{\cdot}6H_2O$, $Ga(NO_3)_3{\cdot}xH_2O$, and NaOH chemicals were used as metal precursors and an oxidation-promoting reactant, respectively. The MWCNTs were prepared by the thermal decomposition of a toluene/ferrocene solution method, which had been described elsewhere.[57] First, MWCNTs were functionalized in a 40 vol% HNO_3 solution at 90-110 °C for 24 h under reflux. Subsequently, a precursor solution was prepared by mixing an equimolar (0.1 M) mixture of cations in HNO_3. The resultant functionalized MWCNTs (*f*-MWCNTs) were mixed with the precursor solution at a 1:0.6 molar ratio for 1 h in an ultrasonic bath. Then, 0.5 M NaOH solution was added slowly under vigorous stirring until the pH reached 7. The resultant suspension was filtered, and the solid product was repeatedly washed with deionized water and dried in open atmosphere at ≈ 80 °C using an infrared lamp. The dried product was heat-treated at 400, 500, and 600 °C in air for 30 min using a heating rate of 5 °C min^{-1}.

Structural, morphological, and chemical characterizations

The structure of the OHNTs was analyzed by XRD (Bruker D8 Advance, with Cu K□ radiation (□=1.5405 Å)), in the scanning range (2□) from 20° to 100 ° with 0.02° step width and constant counting time of 0.6 s/step. The morphology was examined by FE-SEM (JEOL JSM6701F) at an accelerating

voltage of 5 kV using the secondary electron detector. HR-TEM, JEOL ARM200F, at an accelerating voltage of 200 kV in the bright-field mode coupled with scanning transmission electron microscopy (STEM) and EELS, was employed to analyze morphology and element distribution at the nanometer scale. The valence states of OHNTs were investigated by XPS using a Thermo Scientific K-Alpha ESCALAB 250Xi equipped with a 180° double-focusing hemispherical analyzer and a monochromatic Al Kα (1486.6 eV) source. The binding energy scale in the XPS spectra was calibrated to 284.8 eV for the C 1s peak of adventitious carbon. Analysis of the XPS spectra was conducted by using the Thermo Scientific Avantage data system. Raman spectroscopy was used to analyze the nature of covalent bonds using a LabRAM HR Evolution Horiba equipment with a wavelength of 532 nm in the range of 200-3000 cm^{-1}. The oxidation behavior of *f*-MWCNTs and OHNTs in their initial condition was studied by TGA/DTA at 10 °C min^{-1} in an air flow of 50 mL/min, using alumina crucibles (TGA/DTA; Netzsch Regulus 2500 STA).

Photocatalytic evaluation

The photocatalytic activity of OHNTs for the CIP degradation was evaluated in aqueous solutions (10 mg L^{-1}) under UV light irradiation (= 365 nm) without pH adjustment (pH = 7.0). The evaluation was conducted using 50 mg of OHNTs dispersed in 100 mL of the CIP solution. Before the photocatalytic test, the system was maintained in the dark for 30 min to ensure adsorption/desorption equilibrium. The tests were performed at room temperature under constant stirring for 45 min, with aliquots collected every 15 min. The photodegradation efficiency was monitored using a Perkin Elmer UV–vis Lambda 35 Spectrophotometer by measuring the maximum absorption of CIP at 275 nm. The photocatalyst degradation efficiency was calculated using equation (1):

$$\text{Degradation (\%)} = \frac{C_o - C}{C_o} \times 100 \quad (1)$$

where C_o denotes the initial CIP concentration, and C is the CIP concentration at time t of the reaction, respectively. The kinetics of CIP photodegradation were assessed using both pseudo-first order (equation 2) and pseudo-second order (equation 3) models.

$$\ln\left(\frac{C}{C_0}\right) = k_1 \bullet t \tag{2}$$

$$\frac{1}{[C]} = \frac{1}{C_o} + k_2 \bullet t \tag{3}$$

where C_o denotes the initial CIP concentration, and C is the CIP concentration at time t of the reaction. k_1 and k_2 are the rate constants for the models.

Scavenger experiments were conducted on $OHNT_{80}$ to investigate the photocatalytic pathway of CIP degradation. Tert-butanol (20 mM), ethylenediaminetetraacetic acid disodium (EDTA, 5 mM), and $AgNO_3$ (5 mM) were used as radical scavengers to capture hydroxyl radicals (•OH), holes (h^+), and electrons (e^-), respectively. Ascorbic acid (5 mM) acts as a non-selective radical scavenger, quenching superoxide ($O_2^{\bullet -}$) and secondary ROS derived from it.

Optical characterization

The UV-vis DRS was collected using a Perkin Elmer Lambda 950 spectrophotometer equipped with an integrating sphere in the range 200-1100 nm. The PL analysis was performed using a Horiba Scientific Fluorolog FL3–11 instrument with a 450 W short-arc xenon lamp and excitation source 340 nm.

Data availability statement

Data is available on request from the corresponding author, Jorge Roberto Vargas-Garcia, through rvargasga@ipn.mx

References

1. Sham Lal, M., & Sundara, R. High entropy oxides—a cost-effective catalyst for the growth of high yield carbon nanotubes and their energy applications. *ACS Appl. Mater. Interfaces,* **11**, 30846–30857; 10.1021/acsami.9b08794 (2019)
2. Shi, Y., Li, R. & Lei, Z. Influences of synthetic parameters on morphology and growth of high entropy oxide nanotube arrays. *Coatings*. **13**, 46: 10.3390/coatings13010046 (2022)
3. Ran, B., Li, H., Cheng, R., Yang, Z., Zhong, Y., Qin, Y., Yang, C., & Fu, C. High-entropy oxides for rechargeable batteries. *Adv. Sci.* **11**, 2401034: 10.1002/advs.202401034 (2024)
4. Anandkumar, M. & Trofimov, E. Synthesis, properties, and applications of high-entropy oxide ceramics: current progress and future perspectives. *J. Alloys Compd.* **960**, 170690; 10.1016/j.jallcom.2023.170690 (2023)
5. Sun, Y. & Dai, S. High-entropy materials for catalysis: a new frontier. *Sci Adv*. **7**, eabg1600; 10.1126/sciadv.abg1600 (2021)
6. Jia, X. & Li, H. Machine learning enabled exploration of multicomponent metal oxides for catalyzing oxygen reduction in alkaline media- *J. Mater. Chem. A.* **12**, 12487-12500; 10.1039/D4TA01884B (2024)
7. Sarkar, A. et al. Nanocrystalline multicomponent entropy stabilised transition metal oxides. *J. Eur. Ceram. Soc.* **37**. 747-754; 10.1016/j.jeurceramsoc.2016.09.018 (2017)
8. Dąbrowa, J. et al. Synthesis and microstructure of the $(Co,Cr,Fe,Mn,Ni)_3O_4$ high entropy oxide characterized by spinel structure. *Mater. Lett.* **216**, 32-36; 10.1016/j.matlet.2017.12.148 (2018)
9. Sharma, Y. et al. Single-crystal high entropy perovskite oxide epitaxial films. *Phys. Rev. Mater.* **2**, 060404(R); 10.1103/PhysRevMaterials.2.060404 (2018)
10. Cheng, B. et al. Pressure-induced tuning of lattice distortion in a high-entropy oxide. *Commun. Chem.* **2**, 114: 10.1038/s42004-019-0216-2 (2019)
11. Abdul Hai, M., Daud, M., Mujtaba, G., Banat, F. & Al-Harthi, M. A. A comprehensive review of two-dimensional high-entropy layered hydroxides: Synthesis, characterization, and applications. *Coord. Chem. Rev.* **529**, 216435 (2025).
12. Nemani, S. K., Torkamanzadeh, M., Wyatt, B. C., Presser, V. & Anasori, B. Functional two-dimensional high-entropy materials. *Commun. Mater.* **4**, 16 (2023).

13. Okejiri, F. et al. Ultrasound-mediated synthesis of nanoporous fluorite-structured high-entropy oxides toward noble metal stabilization. *iScience.* **25**, 104214; 10.1016/j.isci.2022.104214 (2022)
14. Patriarchi, A. et al. Evaluation of high-entropy (Cr, Mn, Fe, Co, Ni)-oxide nanofibers and nanoparticles as passive fillers for solid composite electrolytes" *Electrochim. Acta.* **512**,145425; 10.1016/j.electacta.2024.145425 (2025)
15. Arun, S.R. & Jacob, G. Exploring the charge storage ability of the spinel-type high entropy oxide $(MnFeCoNiZn)_3O_4$ nanoparticles for supercapacitor applications. *Chem. Eng. J. Adv.* **21**, 100708; 10.1016/j.ceja.2025.100708 (2025)
16. Tian, L., Zhang, Z., Liu, S., Li, G., & Gao, X. High-entropy perovskite oxide nanofibers as efficient bidirectional electrocatalyst of liquid-solid conversion processes in lithium-sulfur batteries. *Nano Energy*. **106**, 108037; 10.1016/j.nanoen.2022.108037 (2023)
17. Asim, M. et al. Microwave synthesis of rock-salt type high entropy oxides immobilized on graphene oxide nanosheets as an efficient catalyst for oxygen evolution reaction. *J. Environ. Chem. Eng.* **13**, 118758;10.1016/j.jece.2025.118758 (2025)
18. Wang, X. et al. Identification of the reconstruction induced high-entropy spinel oxide nanosheets for boosting alkaline water oxygen evolution. *Chem. Eng. J.* **503**, 158488: 10.1016/j.cej.2024.158488 (2025)
19. Wang, X.L., Kim, E.M., Senthamaraikannan, T.G., Lim, D.-H., & Jeong, S.M. Porous hollow high entropy metal oxides $(NiCoCuFeMg)_3O_4$ nanofiber anode for high-performance lithium-ion batteries. *Chem. Eng. J.* **484**, 149509 ;10.1016/j.cej.2024.149509 (2024)
20. Liu, X., Tian, F., Sheng, J., Yu, Y., & Yang, W. High-entropy porous spinel ferrite @ amorphous carbon nanocomposites with abundant structural defects for wide-band electromagnetic wave absorption. *Chem. Eng. J.* **490**, 151848; 10.1016/j.cej.2024.151848 (2024)
21. Zhu, Y., et al. Spinel-type high-entropy oxide nanotubes for efficient oxygen evolution reaction. *Colloids Surf., A*. **686**, 133315; 10.1016/j.colsurfa.2024.133315. (2024)
22. Lei, Z. et al. Ultrastable metal oxide nanotube arrays achieved by entropy-stabilization engineering. *Scr. Mater.* **146**, 340-343; 10.1016/j.scriptamat.2017.12.025 (2018)
23. Musicó, B. L. et al. The emergent field of high entropy oxides: design, prospects, challenges, and opportunities for tailoring material properties. *APL Mater.* **8**, 040912; 10.1063/5.0003149 (2020)

24. Müller, U. Symmetry Relationships between Crystal Structures: Applications of Crystallographic Group Theory in Crystal Chemistry. 217-226 (Springer, 2013).
25. Pacheco-Espinoza, S. et al. Topotactical route to multiwalled cerium oxide nanotubes from MWCNTs. *Part. Part. Syst. Charact.* **40**, 2370007; 10.1002/ppsc.202200167 (2023)
26. Cortés-López, A. J., Muñoz-Sandoval, E., & López-Urías, F. Oxygenated surface of carbon nanotube sponges: electroactivity and magnetic studies. *AMS Omega*. **4**, 18011–18022; 10.1021/acsomega.9b01773 (2019)
27. Dresselhaus, M.S. Endo M. Relation of carbon nanotubes to other carbon materials in *Carbon nanotubes: synthesis, structure, properties, and applications* (Eds.: Dresselhaus, M. S., Dresselhaus, G., Avouris, P.) 11-28 (Springer, 2001)
28. Cahen, S., Speyer, L., Lagrange, P., & Hérold, C. Topotactic mechanisms related to the graphene planes: chemical intercalation of electron donors into graphite. *Eur. J. Inorg. Chem.* **45**, 4798-4806; 10.1002/ejic.201900758 (2019)
29. Wondimu, T. H., Zuo, Y., Shah, A. A., Leung, P. & puiki Leung. The recent progress of high-entropy layered double hydroxides and high-entropy amorphous materials for water electrocatalysis. *Decarb.* **8**, 100110 (2025).
30. Sartoretti, E. et al. In situ Raman analyses of the soot oxidation reaction over nanostructured ceria-based catalysts. *Sci. Rep.* **9**, 3875; 10.1038/s41598-019-39105-5 (2019)
31. McBride, J.R., Hass, K.C., Poindexter, B. D, & Weber, W. H. Raman and x-ray studies of $Ce_{1-x}RE_xO_{2-y}$, where RE = La, Pr, Nd, Eu, Gd, and Tb. *J. Appl. Phys.* **76**, 2435-2441; 10.1063/1.357593 (1994)
32. Sadezky, A., Muckenhuber, H., Grothe, H., Niessner, R., & Pöschl, U. Raman microspectroscopy of soot and related carbonaceous materials: Spectral analysis and structural information. *Carbon*. **43**, 1731-1742; 10.1016/j.carbon.2005.02.018 (2005)
33. Loridant, S. Raman spectroscopy as a powerful tool to characterize ceria-based catalysts. *Catal. Today*. **373**, 98-111; 10.1016/j.cattod.2020.03.044 (2021)
34. Vinodkumar, T., Rao, B.G., & Reddy, B.M. Influence of isovalent and aliovalent dopants on the reactivity of cerium oxide for catalytic applications. *Catal. Today.* **253**, 57-64; 10.1016/j.cattod.2015.01.044 (2015)

35. Agarwal, S., Zhu, X., Hensen, E. J. M., Lefferts, L., & Mojet, B.L, Defect chemistry of ceria nanorods. *J. Phys. Chem. C.* **118**, 4131–4142; 10.1021/jp409989y (2014)
36. Li, L., Chen, F., Lu, J.-Q., & Luo, M.-F. Study of defect sites in $Ce_{1-x}MxO_{2-\delta}$ ($x = 0.2$) solid solutions using Raman spectroscopy. *J. Phys. Chem. A.* **115**, 7972–7977; 10.1021/jp203921m (2011)
37. Rudolph, W. W. & Irmer, G. Raman spectroscopic characterization of light rare earth ions: La^{3+}, Ce^{3+}, Pr^{3+}, Nd^{3+} and Sm^{3+} – hydration and ion pair formation. *Dalton Trans.* **46**, 4235–4244 (2017).
38. Schweke, D., Rubin, A., Rabinovitch, L., Kraynis, O. & Livneh, T. Cerium metal oxidation studied by IR reflection-absorption and Raman scattering spectroscopies. *J. Phys.: Condens. Matter* **34**, 324002 (2022).
39. Vanpoucke, D.E.P., Bultinck, P., Cottenier, S., Van Speybroeck, V., & Van Driessche, I. Aliovalent doping of CeO_2: DFT study of oxidation state and vacancy effects. *J. Mater. Chem. A*. **2**, 13723-13737; 10.1039/C4TA02449D (2014)
40. Matussin, S.N., Khan, F., Harunsani, M. H., Kim, Y. M., & Khan, M. M. Visible-light-induced photocatalytic and photoantibacterial activities of Co-doped CeO_2. *ACS Omega.* **8**, 11868–11879; 10.1021/acsomega.2c07058 (2023)
41. Chidaraboyina, S., Nesaraj, A. S., & Arunkumar, M. Aluminium doped cerium oxide as an efficient nanophotocatalyst for the elimination of rhodamine B dye present in water. *Asian J. Chem.* **35**, 882-886; 10.14233/ajchem.2023.27574 (2023)
42. Ramasamy, V., Mohana, V., & Suresh, G. Study of Ni:CeO_2 nanoparticles for efficient photodegradation of methylene blue by sun light irradiation. *Indian J. Phys.* **92**, 1601–1612: 10.1007/s12648-018-1246-9 (2018)
43. Wang, F., et al. Ga-doped CeO_2 nanorods as highly active catalysts for the synthesis of dimethyl carbonate from CO_2 and methanol. *React. Kinet., Mech. Catal.* **136**, 2941–2954; 10.1007/s11144-023-02506-9 (2023)
44. Ghobadi, A., Ghobadi, T.G.U., Karadas, F., & Ozbay, E. Angstrom thick ZnO passivation layer to improve the photoelectrochemical water splitting performance of a tio_2 nanowire photoanode: the role of deposition temperature. *Sci. Rep.* **8**, 16322; 10.1038/s41598-018-34248-3 (2018)
45. Song, X. & Boily, J.-F. Surface and Bulk Thermal Dehydroxylation of FeOOH Polymorphs. *J. Phys. Chem.* A **120**, 6249–6257 (2016).

46. Gager, E. & Nino, J. C. Processing, phase stability, and conductivity of multication-doped ceria. *Inorganics*. **11**, 299; 10.3390/inorganics11070299 (2023)
47. Lv, N., Lin, S., Ding, L, Qi, K., Zhang, W., Popkov, V. Interfacial charge transfer in $Ti_3C_2O_2$/NLCOF heterojunction enables efficient photocatalytic H_2O_2 production. *Chemical Engineering Journal*. **522**, 167143; 10.1016/j.cej.2025.167143 (2025)
48. Chenakin, S.P., Prada Silvy, R., Kruse, N. XPS–SIMS surface characterization of aluminovanadate oxide catalyst precursors co-precipitated at different pH: effect of calcination. *Topics in Catalysis*. **55**, 731–746; 10.1007/s11244-012-9872-5 (2012)
49. Na, S., Shi, X., Chai, D.F., Guo, D., Li, J. Synergistic hybridization between third-period and fifth-period transition metal orbitals in entropy-stabilized layered double hydroxides for long-term oxygen evolution catalysis. *Journal of Colloid and Interface Science.* **693**, 137641; 10.1016/j.jcis.2025.137641 (2025)
50. Scheibe, B., Borowiak-Palen, E., & Kalenczuk, R.J. Oxidation and reduction of multiwalled carbon nanotubes — preparation and characterization. *Mater. Charact.* **61**, 185-191; 10.1016/j.matchar.2009.11.008 (2010)
51. Li, Y.X., Zhou, X.Z., Wang, Y., & You, X.Z. Preparation of nano-sized CeO_2 by mechanochemical reaction of cerium carbonate with sodium hydroxide. *Mater. Lett.* **58**, 245-249; 10.1016/S0167-577X(03)00454-3 (2004)
52. Ansari, A.A. & Kaushik, A. Synthesis and optical properties of nanostructured $Ce(OH)_4$. *J. Semicond.* **31**, 033001; 10.1088/1674-4926/31/3/033001 (2010)
53. Weiss, T. P., Bissig, B., Feurer, T., Carron, R., Buecheler, S. & Tiwari, A. N. Bulk and surface recombination properties in thin film semiconductors with different surface treatments from time-resolved photoluminescence measurements. *Sci. Rep.* **9**, 5385; 10.1038/s41598-019-41716-x (2019)
54. Queiróz, A.C.B. et al. Ciprofloxacin photodegradation by CeO_2 nanostructures with different morphologies. *Water, Air, Soil Pollut.* **234**, 415: 10.1007/s11270-023-06424-3 (2023)
55. H. Yao, Q. Li, Y. Gao, et al. Revealing effect of surface hydroxyl variation on charge spatiotemporal dynamics in photocatalysis. *J. Am. Chem. Soc*. **147**, 23308–23317; 10.1021/jacs.5c08206 (2025).
56. Ajin, V. C. Antony & Lenus, A. Jestin. Engineering the role of oxygen vacancies in photocatalysts for environmental remediation and energy

conversion applications: A comprehensive review. *Mater. Sci. Semicond. Process.* **197**, 109705; 10.1016/j.mssp.2025.109705 (2025)

57. Andrews, R. et al. Continuous production of aligned carbon nanotubes: a step closer to commercial realization. *J. Chen, Chem. Phys. Lett.* **303**, 467-474; 10.1016/S0009-2614(99)00282-1 (1999)

Acknowledgments

This work was supported by the National Polytechnic Institute of Mexico (IPN-SIP 20250896 and IPN-SIP 20250084) and SECIHTI (CBF-2025-I-2873). Sarahi Pacheco-Espinoza acknowledges financial support for postdoctoral grant.

Funding

The Authors received FUNDING for this work:
M.A. H.-P., Instituto Politécnico Nacional, México, IPN-SIP 20250084.
J.R. V.-G., Instituto Politécnico Nacional, México, IPN-SIP 20250896.
J.R. V.-G., Secretaría de Ciencia, Humanidades, Tecnología e Innovación, México, CBF-2025-I-2873.

Author contributions

Sarahi Pacheco-Espinoza: Conceptualization, Investigation, Validation, Writing – original draft. **María Ángeles Hernández-Pérez:** Supervision, Project Administration, Validation, Founding Acquisition, Writing – review & editing. **Alejandro Iván Cuesta-Balderas:** Methodology, Investigation, Data curation, Writing-original draft. **Alejandra Verdejo-Palacios**: Methodology, Investigation, Data curation, Writing-original draft. **Raúl Borja-Urby:**

Methodology, Investigation, Data curation, Writing-original draft. **Jorge Roberto Vargas-García:** Supervision, Project Administration, Validation, Founding Acquisition, Writing – review & editing.

Competing interests

The authors declare no competing interests.

Figure captions

Figure 1. a) XDR patterns of *f*-MWCNTs and OHNTs, b) deconvolution analysis of C (002) and OHNTs (111) XRD peaks.

Figure 2. HR-TEM images of a) *f*-MWCNTs, b-c) $OHNT_{400}$, and d) EELS elemental mapping image.

Figure 3. a) Raman spectra of *f*-MWCNTs and OHNTs, b) deconvolution analysis of the F_{2g} band.

Figure 4. a) Survey spectra for OHNTs, b) high-resolution C 1s spectra for *f*-MWCNTs and OHNTs, c) Ce 3d spectra for OHNTs, d) O 1s spectra for OHNTs, and e) O_V concentration.

Figure 5. a) TGA curves of *f*-MWCNTs and OHNTs in their as-prepared condition, and b) DTA curve of OHNTs

Figure 6. SEM images of the OHNTs morphological evolution.

Figure 7. a) Efficiency of OHNTs in photocatalytic CIP degradation, kinetic of CIP degradation using b) pseudo-first order model and c) pseudo-second order model, d) effect of radical scavengers on CIP degradation, e) UV-vis DRS reflectance spectra of $OHNT_{80}$ and $OHNT_{600}$, and f) PL spectra of $OHNT_{80}$ and $OHNT_{600}$.

Figure 8. The degradation mechanisms for $OHNT_{80}$ and $OHNT_{600}$.

Table caption

Table 1. Identification of samples.